6 Supplementary Materials

6.1 Study region sea ice regime

Video S1 <*Vic_Strait_Sent_1_2016_2017.avi*> shows a time sequence of Sentinel-1 GRD images over the Victoria Strait region from July 2016 to October 2017. The sea ice began freezing North of Victoria Island, in M'Clintock Channel, where some MYI floes were present (mid-October 2016). Ice formed near land and spread throughout the southern portion of the study region, while open water in M'Clintock Channel and leads in Victoria Strait persisted. Areas of smooth ice formed and persisted in wind- and current-sheltered areas (e.g., part of M'Clintock Channel and Queen Maud Gulf). Victoria Strait showed north-south axis movement of sea ice, and underwent ice deformation processes that continued late into winter, resulting in very rough sea ice. In spring, the sea ice began breaking at the northern and southern edges of Victoria Strait, and the ice in the strait began forming large leads. Open water then formed near land, before appearing in the south and moving northwards.

6.2 HH backscatter processing

We processed 17 Sentinel-1 HH-band extra wide swath (EW) scenes captured between 12 March and 15 April 2017 during cold conditions, when the backscatter contribution from sea ice is stable and differences in backscatter between images are due to changes in incidence angle. Image processing consisted of i) thermal noise removal; ii) calibration (both Sigma-nought and Gamma-nought); iii) speckle filtering (Lee 5×5), and iv) map projection. Backscatter statistics and incidence angle were calculated for two FYI regions of interest (ROIs) (19.6 km^2 and 17.6 km^2) and three MYI ROIs (7.5 km^2, 9.8 km^2, and 19.7 km^2). Results from this analysis are shown in Fig. S1. We chose to use a gamma-nought calibration for the roughness comparisons in order to reduce sensitivity to incidence angle (Fig. S1) (Dierking and Busche, 2006; Dierking and Dall, 2007). Alternatively, some other studies opt to adjust SAR images to remove the effects of incidence angle on backscatter, either by applying scaling or corrections using backscatter from dark and light reference areas (Melling, 1998; Makynen and others, 2002; Martinez-Agirre and others, 2017; Gegiuc and others, 2018).

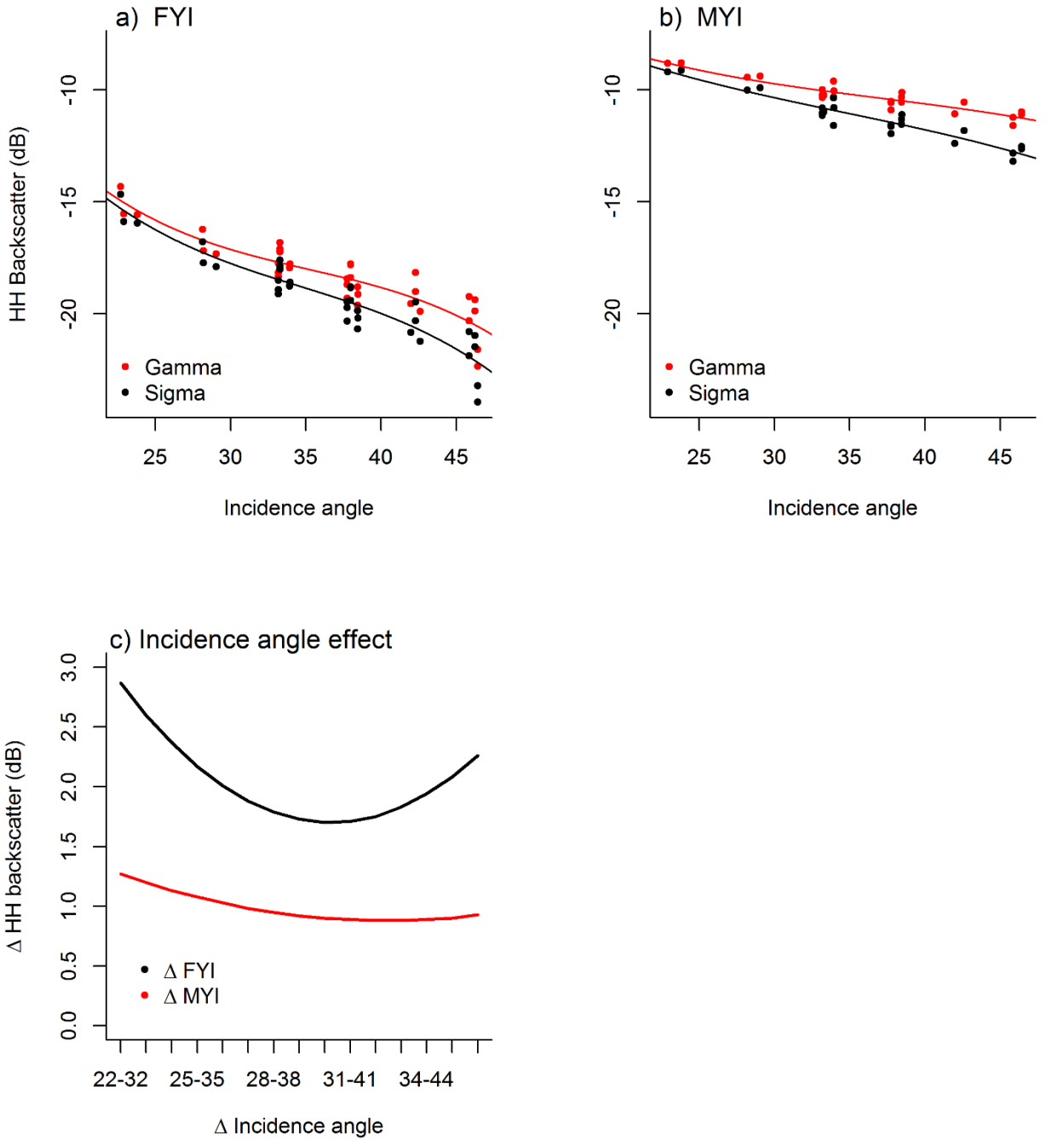

Fig. S1. Sentinel-1 HH-band backscatter from a) FYI and b) MYI targets, given as cubic functions of incidence angle for gamma-nought and sigma-nought calibrations. The effect of incidence angle is less for gamma-nought calibration and is similar between FYI and MYI types. In c) the effect of ten-degree incidence angle intervals is shown as HH gamma nought backscatter ranges, for FYI and MYI types.

Table S1. Information about the sensors and products used to investigate the effect of incidence angle on Sentinel-1 backscatter over FYI and MYI in M'Clintock Channel, winter 2017.

Platform	**Payload**	**Date** (dd-mmm-yy)	**Dir/Mode**	**Orbit (Track)**	**ID**	**Format**
S1A	SAR-C	16-Mar-17	Des/EW	15718 (71)	CC2C	GRD
S1A	SAR-C	16-Mar-17	Des/EW	15718 (71)	661C	GRD
S1A	SAR-C	20-Mar-17	Des/EW	15776 (129)	E279	GRD
S1A	SAR-C	09-Apr-17	Des/EW	15776 (129)	DFD1	GRD
S1A	SAR-C	11-Apr-17	Des/EW	16097 (100)	E3EA	GRD
S1B	SAR-C	12-Mar-17	Des/EW	4676 (100)	7B4F	GRD
S1B	SAR-C	14-Mar-17	Des/EW	4705 (129)	4ACF	GRD
S1B	SAR-C	17-Mar-17	Des/EW	4749 (173)	0AE8	GRD
S1B	SAR-C	22-Mar-17	Asc/EW	4822 (71)	F378	GRD
S1B	SAR-C	26-Mar-17	Asc/EW	4880 (129)	74C6	GRD
S1B	SAR-C	27-Mar-17	Asc/EW	4895 (144)	B970	GRD
S1B	SAR-C	29-Mar-17	Asc/EW	4924 (173)	55F6	GRD
S1B	SAR-C	31-Mar-17	Asc/EW	4953 (27)	0B83	GRD
S1B	SAR-C	01-Apr-17	Asc/EW	4968 (42)	6869	GRD
S1B	SAR-C	10-Apr-17	Asc/EW	5099 (173)	B132	GRD
S1B	SAR-C	12-Apr-17	Asc/EW	5128 (27)	2A30	GRD
S1B	SAR-C	15-Apr-17	Asc/EW	5172 (71)	DA2D	GRD

Abbreviations are as follows: S = Sentinel; Des = descending; Asc = ascending; EW = extended wide-swath; GRD = ground range detected.

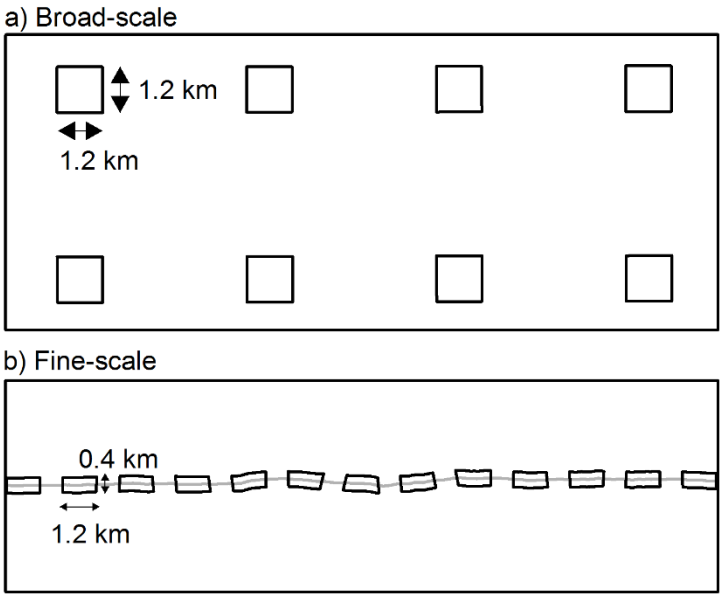

Fig. S2. Schematic showing a) a subset of the broad-scale grid, and b) a subset of the fine-scale grid. In the latter, the LiDAR flight path is shown in grey.

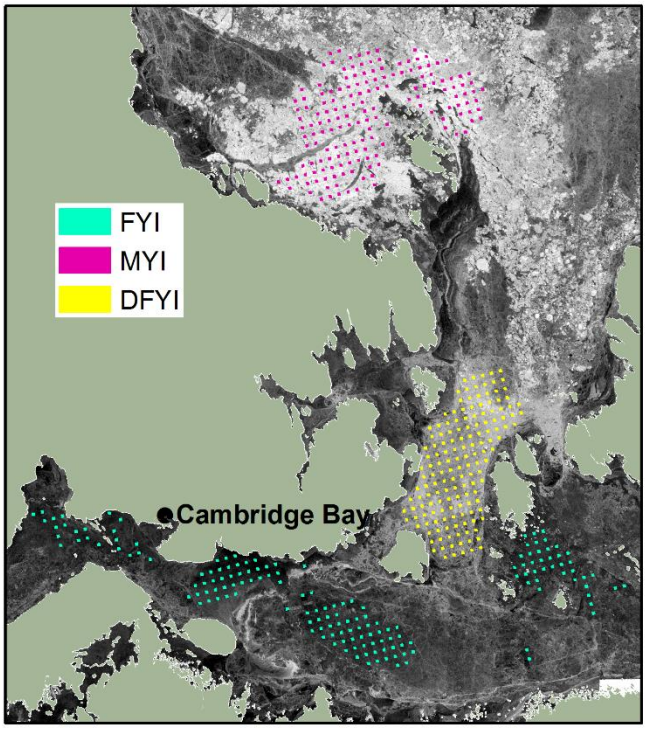

Fig. S3. Locations of grid cells assigned to FYI (blue), MYI (purple), and DFYI (yellow) categories in the broad-scale dataset.

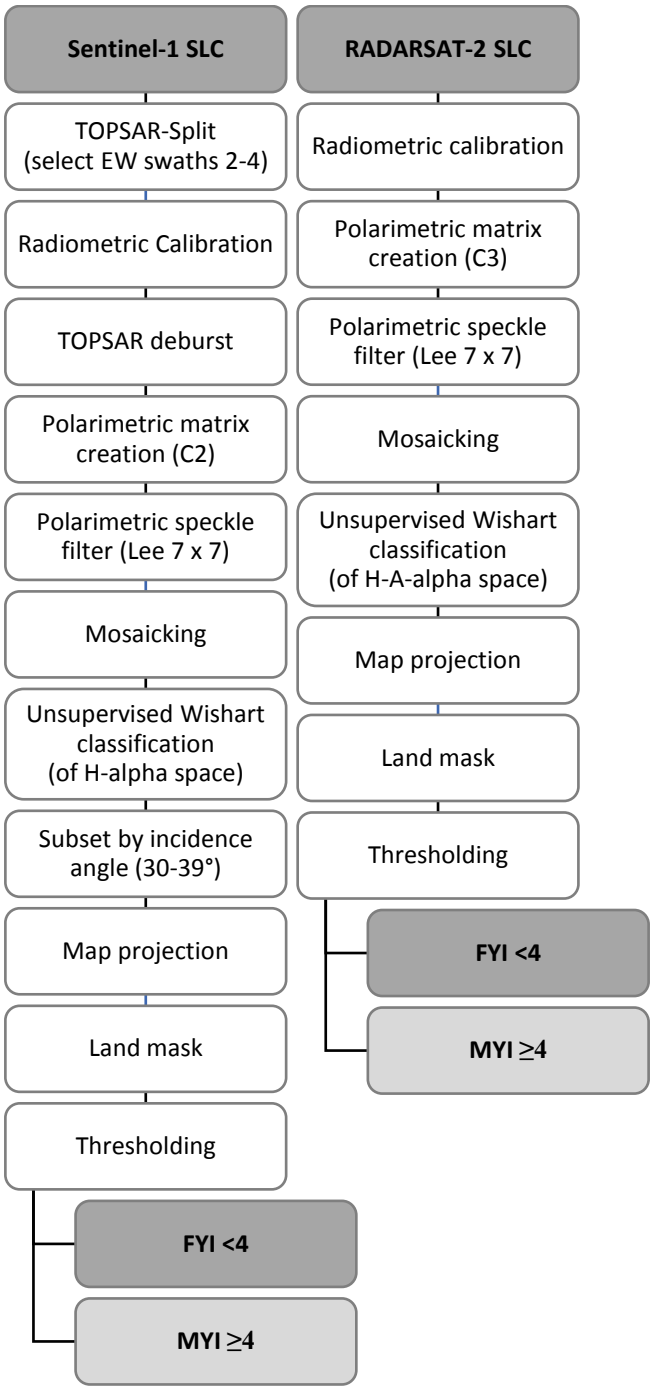

Fig. S4. Schematic showing Sentinel-1 and RADARSAT-2 data pre-processing (top to bottom) for data used in MYI classification. Processing is also described in Section 2.4.

6.3 NDAI and HH backscatter relationships by ice type

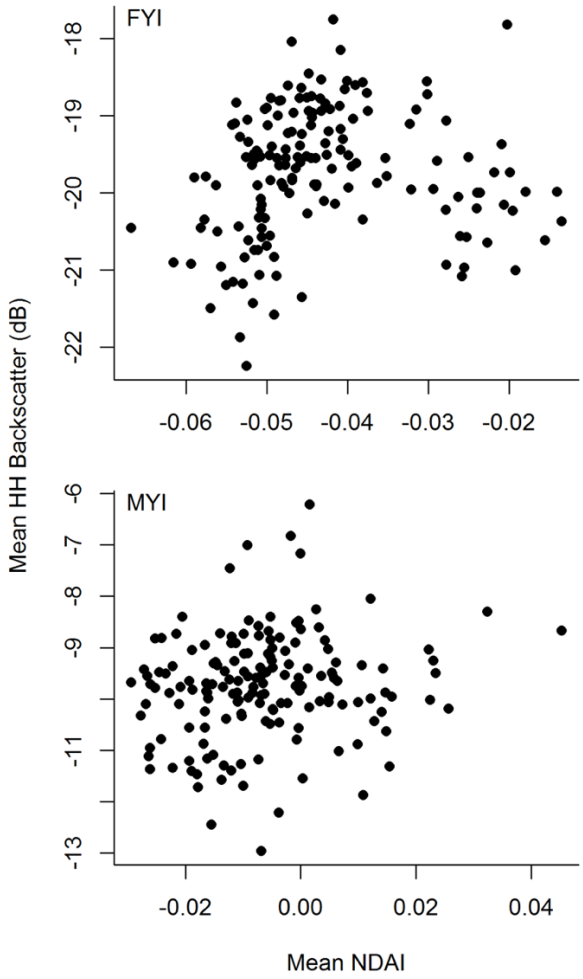

Fig. S5. Scatterplot showing Sentinel-1 HH backscatter and mean MISR NDAI for FYI (top) and MYI (bottom) types.

6.4 HH backscatter by region

Table S2. FYI C-band HH backscatter observed across Arctic roughness regimes.

Region	**FYI**		**Rough FYI**		**Incidence angle**[1]	**Source**
	Backscatter (dB)	***Value description***	***Backscatter (dB)***	***Value description***		
Kitikmeot	-18.53 -19.7 -22.2 to -19.7	FYI median FYI mean FYI range	-13.49 -13.3 -17.6 to -10.2	DFYI median DFYI mean DFYI range	30-40°	*(This study)*
Cornwallis Island, Nunavut	-19.3	FYI mean	-16.1	Rough FYI mean	26.0-45.2°	*(Geldsetzer and Yackel, 2009)*
Franklin Bay, Northwest Territories	-20.45 -21-74	FYI mean	-11.73 -12.23 -9.66 -10.12	Rough FYI[2] mean DFYI[3] mean	31-33° 35-37° 31-33° 35-37°	*(Gill and Yackel, 2012)*
Beaufort Sea/ Amundsen Gulf	-23 to -19	FYI range	-14 to -13	DFYI range	30-40°	*(Gupta and others, 2014)*
Beaufort Sea/ Amundsen Gulf	-22 to -18	FYI range	-14 to -13	DFYI range	30-40°	*(Gupta and others, 2013)*
Eastern Beaufort Sea	~-22 to -19.8	FYI range	~-12.5	FYI ridge range	20.1-25.9°	*(Melling, 1998)*
Southwestern Hudson Bay	-13 -15	FYI mean	-10 -7.5 -11.5 -9	Rough FYI mean DFYI mean Rough FYI mean DFYI mean	29° 29° 39° 39°	*(Hossain and others, 2014)*
Svalbard Fram Strait Barents Sea	-15 to -7.5 -14.5 to -9 -16.5 to -10	FYI range	-11 to -4.5 -6.5 to -4 -11.5 to -6.5	Broken ice range FYI ridge range Brash/rubble range	30-45°	*(Dierking, 2010)*
Baltic Sea	~ -19 (data points all < -16.5)	Model predictions of >80% level ice	~ -12 (data points all > -17)	Model predictions of <20% level ice	23.2-25.3°; 40.3-42.5°	*(Similä and others, 2010)*
Baltic Sea	-20 -25 -16 -14	Dry snow; FYI Wet snow; FYI	-17 -21 -13 -17 -10 -13 -12 -11 -11 -11	Dry snow, rough FYI Dry snow, slightly DFYI[4] Dry snow, highly DFYI[5] Wet snow, slightly DFYI Wet snow, highly DFYI	23° 45° 23° 45° 23° 45° 23° 45° 23° 45°	*(Mäkynen and Hallikainen, 2004)*
Baltic Sea	-15	FYI mean	-9	DFYI mean	45°	*(Dierking and Dall, 2007)*
Baltic Sea	-13.5 to -11 -16.25 to -14.25	FYI range	-8.25 to -7 -12.5 to -9.5	Rough fast FYI mean	20° 33°	*(Eriksson and others, 2010)*
Baltic Sea	-21.5 to -10 -21.5 to -10 -21 to -5	FYI range from proportion of observations >0.05 (Jan.) (Feb.) (Mar.)	-19.5 to -19; -18.5 to -11.5 -16 to -10.5 -17 to -11	Ridged ice range from proportion of observations >0.05 (Jan.) (Feb.) (Mar.)	20-49° (corrected)	*(Gegiuc and others, 2018)*

[1] Limited to 30-40° if possible
[2] Broken or uneven FYI with protruding blocks and/or edges
[3] Rubble ice, ridges, and/or boulders >1m in size
[4] Contains ice ridges and uneven surfaces; level ice components in this zone are usually >100m
[5] Level ice components usually <100m, with lower proportional area than DFYI

6.5 Other data and recommendations (continued)

Radar systems are sensitive to the sea ice surface at scales of the radar wavelength: the C-band wavelength is ~5.7 cm, L-band ~23.6 cm, and X-band ~3.1 cm (Richards, 2009). Several studies using the longer L-band wavelength have found that deformation features have a higher contrast to smooth ice than higher frequencies and are less sensitive to small-scale roughness, ice type, and spring conditions (Dierking and Busche, 2006; Arkett and others, 2008; Eriksson and others, 2010). L-band HH polarization at larger incidence angles (35-42°) was found to be particularly useful for characterizing surface deformation, and detected a higher fractional area of DFYI than C-band SAR in the Baltic Sea (Dierking and Busche, 2006; Dierking and Dall, 2007), likely because C-band backscatter is very sensitive to small-scale (several wavelength) deformations, which can obscure larger-scale features (Dierking and others, 1997), and makes the contrast between level and deformed ice at L-band higher for small height undulations (e.g., rafted ice) (Dierking and Dall, 2007). L-band SAR has also proven useful during freeze-up, as the frequency is less sensitive to new ice frost-flower roughness and thus backscatter and texture are more related to ice thickness (and larger-scale roughness) (Arkett and others, 2008).

Shorter wavelength X-band SAR is more sensitive to snow and air bubbles in the upper ice layer than lower frequencies, responding with higher volume scattering and consequently shallower penetration into the sea ice (Richards, 2009; Eriksson and others, 2010). This frequency separates level FYI and level MYI from new and young ice more easily than lower frequencies and has greater contrast between sea ice and calm water, making it sensitive to spring melt (Eriksson and others, 2010). The main differences between X- and C-band frequencies are at micro-scale surface interactions (mm-cm; to which L-band is less sensitive), rather than differences related to macro-scale roughness (Richards, 2009; Eriksson and others, 2010). Eriksson et al. (2010) found that co-pol backscatter from X-band appeared similar to C-band, and cross-pol X-band data similar to L-band, with deformation features easier to recognize at L-band than at X-band. While X- and C-band datasets (but not L-band) provide similar information (Mäkynen and Hallikainen, 2004; Eriksson and others, 2010), several studies report that multifrequency data is helpful for identifying roughness (Arkett and others, 2008; Eriksson and others, 2010; Milillo and others, 2015). For example, ice blocks >30 cm on relatively level ice could be identified by their high backscatter across X-, C- and L-band, while smooth level ice exhibited reduced backscatter at lower frequencies (Eriksson and others, 2010). Consequently, access to multiple frequencies would provide more information for community sea ice maps. Unfortunately, the cost (L-and X-band), low temporal resolution (L-band) and small swath size (X-band) of the current X- and L-band satellites makes their current utility for frequent and large-scale data collection limited. Region-based subscription offered by companies like ICEYE, Planet and DigitalGlobe, may prove to be more cost-effective options for monitoring sea ice near particular communities.

Multiple SAR polarization parameters can also have utility for discriminating rough sea ice from level ice, or for identifying degrees of deformation. Studies have found that multiple C-band channel combinations (Drinkwater and others, 1992; Gill and Yackel, 2012), cross-pol ratios (Dierking and Dall, 2007; Gegiuc and others, 2018), co-pol ratios (Dierking and Dall, 2007; Johansson and others, 2017), and other measures of depolarization, intensity, decomposition, etc., can contain information about roughness (Moen and others, 2013; Hossain and others, 2014; Casey and others, 2014; Brekke and others, 2015; Fors and others, 2016), though it remains necessary to interpret the data in the context of seasonal and ice/snow properties (Fors and others, 2015). While multiple polarization parameters can increase the

effectiveness of roughness mapping, there is evidence that the HH channel works well for detecting rough sea ice and is generally as strong as any other single metric (Gill and Yackel, 2012; Fors and others, 2015; Xu and others, 2017; Gegiuc and others, 2018).

Other data types, including multi-angle and stereo-pair optical data, can also provide information on sea ice elevation and roughness. MISR and other optical satellites (e.g., DigitalGlobe's WorldView-1-4, GeoEye-1) or platforms (e.g., airborne or UAV) can capture multiple off-nadir images from one platform or from coincident but separate orbits, allowing for the creation of digital elevation and roughness models (Shean and others, 2016; Dammann and others, 2018; Li, 2018). Fine-scale optical datasets can also assess roughness using ice feature shadows (Zakharov and others, 2015). However, most multi-angle and high-resolution optical images are only commercially available (Table S3). Other methods of obtaining sea ice roughness include CryoSat-2 radar altimetry (Shepherd and others, 2012; Kurtz and others, 2014), although backscatter angle can cause roughness errors. ICESat laser altimetry measures elevation, but ellipsoidal coverage is not continuous and is affected by the roughness found within each ellipse (Kurtz and others, 2008). Scatterometers are sensitive to surface roughness, among other parameters (Nghiem and others, 2007; Remund and Long, 2014; Gupta, 2015).

Table S3. Current and near-future satellite-based payloads that may be useful (high quality and/or affordable) for providing sea ice surface trafficability information to northern communities.

Data Type	Programme(s) and relevant payloads	Agency	Availability	Example roughness studies
C-band SAR	Sentinel-1 (SAR-C)	ESA, EC	Open access	*(Dierking, 2010; Martinez-Agirre and others, 2017)*
C-band SAR	RADARSAT-2 (SAR)	CSA	Restricted	*(Gauthier and others, 2010; Ersahin and others, 2014; Hossain and others, 2014; Brekke and others, 2015; Mussells, 2015; Zakharov and others, 2015; Fors and others, 2016; Johansson and others, 2017; Xu and others, 2017; Gegiuc and others, 2018)*
C-band SAR	RADARSAT Constellation Mission (SAR RCM)	CSA	Restricted	*(Nasonova and others, 2018)*
X-band SAR	TerraSAR-X (SAR-X) and TanDEM-X (SAR-X)	DLR	Restricted	*(Zakharov and others, 2015; Linow, 2015; Johansson and others, 2017; Dammann and others, 2018; Yitayew and others, 2018)*
X-band SAR	COSMO-SkyMed (SAR-2000)	ASI	Restricted	
X-band SAR	ICEYE-X1	ICEYE	Restricted	
X-band SAR	SEOSAR/Paz (SAR-X)	CDTI	Restricted	
L-band SAR	ALOS-2 (PALSAR-2)	JAXA	Restricted	*(Johansson and others, 2017; Dammann and others, 2018)*
X- and L-band SAR, Panchromatic, Multispectral, NIR; RGB video	OptiSAR, Deimos-1 -2 (SLIM6, HIRAIS); Theia, Iris	Urthecast	Restricted	
Multispectral	Terra (ASTER, MISR)	NASA	Open access	*(Nolin and Mar, 2019; Nolin and Payne, 2007; Nolin and others, 2002; Wu and others, 2009; Chust and Sagarminaga, 2007)*
Multispectral	Sentinel-2 (MSI)	ESA, EC	Open access	
Panchromatic and multispectral	DigitalGlobe Constellation (WorldView-1-4: WV60, WV110, WV110, SpaceView-110; and GeoEye-1: GIS)	DigitalGlobe	Restricted	*(Brekke and others, 2015; Zakharov and others, 2015; Shean and others, 2016)*
Multispectral, RGB, and NIR	RapidEye (REIS); SkySat-1; SkySat-2; SkySat-3; SkySat-5; SkySat-6; SkySat-7; Flock-2e; Flock-2e'; Flock-2p; Flock-3p	Planet	Restricted	
Altimeter	Sentinel-3 (SRAL)	ESA, EC, EUMETSAT	Open access	

6.6 Supplementary Material References

Arkett M, Flett D, Abreu RD, Clemente-Colon P, Woods J and Melchior B (2008) Evaluating ALOS-PALSAR for ice monitoring - what can L-band do for the North American Ice Service? *IGARSS 2008 - 2008 IEEE International Geoscience and Remote Sensing Symposium*. V-188-V–191. doi: 10.1109/IGARSS.2008.4780059.

Brekke C, Grahn J and Doulgeris AP (2015) Quad-polarimetric SAR for roughness and deformation characterization of sea ice at Hopen. *Proceedings of POLinSAR 2015*. Frascati, Italy http://www.npcarcticpotentialreport.org/pdf/tp/5-5_Summary_of_Current_Ice_Characterization_Research-Norway-Russia-Europe.pdf.

Casey JA, Beckers J, Busche T and Haas C (2014) Towards the retrieval of multi-year sea ice thickness and deformation state from polarimetric C- and X-band SAR observations. *2014 IEEE Geoscience and Remote Sensing Symposium*. 1190–1193. doi: 10.1109/IGARSS.2014.6946644.

Chust G and Sagarminaga Y (2007) The multi-angle view of MISR detects oil slicks under sun glitter conditions. *Remote Sensing of Environment* **107**(1–2), 232–239. doi: 10.1016/j.rse.2006.09.024.

Dammann DO, Eicken H, Mahoney AR, Saiet E, Meyer FJ and George JC "Craig" (2018) Traversing sea ice: Linking surface roughness and ice trafficability through SAR polarimetry and interferometry. *IEEE Journal of Selected Topics in Applied Earth Observations and Remote Sensing* **PP**(99), 1–18. doi:10.1109/JSTARS.2017.2764961.

Dierking W (2010) Mapping of different sea ice regimes using images from Sentinel-1 and ALOS synthetic aperture radar. *IEEE Transactions on Geoscience and Remote Sensing* **48**(3), 1045–1058. doi: 10.1109/TGRS.2009.2031806.

Dierking W and Busche T (2006) Sea ice monitoring by L-band SAR: an assessment based on literature and comparisons of JERS-1 and ERS-1 imagery. *IEEE Transactions on Geoscience and Remote Sensing* **44**(4), 957–970. doi: 10.1109/TGRS.2005.861745.

Dierking W, Carlstrom A and Ulander LMH (1997) The effect of inhomogeneous roughness on radar backscattering from slightly deformed sea ice. *IEEE Transactions on Geoscience and Remote Sensing* **35**(1), 147–159. doi: 10.1109/36.551943.

Dierking W and Dall J (2007) Sea-ice deformation state from synthetic aperture radar imagery—Part I: Comparison of C- and L-band and different polarization. *IEEE Transactions on Geoscience and Remote Sensing* **45**(11), 3610–3622. doi: 10.1109/TGRS.2007.903711.

Drinkwater MR, Kwok R, Rignot E, Israelsson H, Onstott RG and Winebrenner (1992) Potential applications of polarimetry to the classification of sea ice. Carsey FD ed. *Microwave remote sensing of sea ice*. American Geophysical Union, Washington DC, 419–430.

Eriksson LEB, Borenäs K, Dierking W, Berg A, Santoro M, Pemberton P, Lindh H and Karlson B (2010) Evaluation of new spaceborne SAR sensors for sea-ice monitoring in the Baltic Sea. *Canadian Journal of Remote Sensing*, **36**(sup1), S56-S73. doi: 10.5589/m10-020.

Ersahin K, Brown L, Kanwar A, Henley M, Ross E and Fissel D (2014) Characterization of hazardous ice using spaceborne SAR and ice profiling sonar: preliminary results. Offshore Technology Conference, OTC-24600-MS. Houston TX. doi: 10.4043/24600-MS.

Fors AS, Brekke C, Gerland S, Doulgeris AP and Beckers JF (2016) Late summer Arctic sea ice surface roughness signatures in C-Band SAR data. *IEEE Journal of Selected Topics in Applied Earth Observations and Remote Sensing* **9**(3), 1199–1215. doi: 10.1109/JSTARS.2015.2504384.

Fors AS, Brekke C, Gerland S, Doulgeris AP and Eltoft T (2015) Extraction of late summer sea ice properties from polarimetric SAR features in C-and X-band. *Proceedings of POLinSAR 2015*. Frascati, Italy, ESA SP-729.

Gauthier Y, Tremblay M, Bernier M and Furgal C (2010) Adaptation of a radar-based river ice mapping technology to the Nunavik context. *Canadian Journal of Remote Sensing* **36**(S1), S168–S185. doi: 10.5589/m10-018.

Gegiuc A, Similä M, Karvonen J, Lensu M, Mäkynen M and Vainio J (2018) Estimation of degree of sea ice ridging based on dual-polarized C-band SAR data. *The Cryosphere* **12**(1), 343–364. doi: 10.5194/tc-12-343-2018.

Geldsetzer T and Yackel JJ (2009) Sea ice type and open water discrimination using dual co-polarized C-band SAR. *Canadian Journal of Remote Sensing* **35**(1), 73–84. doi: 10.5589/m08-075.

Gill JPS and Yackel JJ (2012) Evaluation of C-band SAR polarimetric parameters for discrimination of first-year sea ice types. *Canadian Journal of Remote Sensing* **38**(3), 306–323. doi: 10.5589/m12-025.

Gupta M (2015) Various remote sensing approaches to understanding roughness in the marginal ice zone. *Physics and Chemistry of the Earth, Parts A/B/C* **83–84**, 75–83. doi: 10.1016/j.pce.2015.05.003.

Gupta M, Barber DG, Scharien RK and Isleifson D (2014) Detection and classification of surface roughness in an Arctic marginal sea ice zone: Surface roughness in MIZ. *Hydrological Processes* **28**(3), 599–609. doi: 10.1002/hyp.9593.

Gupta M, Scharien RK and Barber DG (2013) C-band polarimetric coherences and ratios for discriminating sea ice roughness. *International Journal of Oceanography* **2013**(567182), 1–13. doi: 10.1155/2013/567182.

Hossain M, Yackel J, Dabboor M and Fuller MC (2014) Application of a three-component scattering model over snow-covered first-year sea ice using polarimetric C-band SAR data. *International Journal of Remote Sensing* **35**(5), 1786–1803. doi: 10.1080/01431161.2013.879345.

Johansson AM, King JA, Doulgeris AP, Gerland S, Singha S, Spreen G and Busche T (2017) Combined observations of Arctic sea ice with near-coincident colocated X-band, C-band, and L-band SAR satellite remote sensing and helicopter-borne measurements. *Journal of Geophysical Research: Oceans* **122**(1), 669–691. doi: 10.1002/2016JC012273.

Kurtz NT, Galin N and Studinger M (2014) An improved CryoSat-2 sea ice freeboard retrieval algorithm through the use of waveform fitting. *The Cryosphere* **8**(4), 1217–1237. doi: 10.5194/tc-8-1217-2014.

Kurtz NT, Markus T, Cavalieri DJ, Krabill W, Sonntag JG and Miller J (2008) Comparison of ICESat data with airborne laser altimeter measurements over Arctic sea ice. *IEEE Transactions on Geoscience and Remote Sensing* **46**(7), 1913–1924. doi: 10.1109/TGRS.2008.916639.

Li Y (2018) Sea ice and ice sheet surface roughness characterization and its effects on bi-directional reflectance. Thesis, Texas A & M University, College Station, Texas. https://oaktrust.library.tamu.edu/handle/1969.1/173578.

Linow S (2015) What can polarimetric SAR data tell us about snow accumulation on polar ice sheets? Presentation, *POLinSAR 2015*, 26-30 January 2015. Frascati, Italy. https://www.researchgate.net/publication/272348126_What_can_polarimetric_SAR_data_tell_us_about_snow_accumulation_on_polar_ice_sheets.

Mäkynen M and Hallikainen M (2004) Investigation of C- and X-band backscattering signatures of Baltic Sea ice. *International Journal of Remote Sensing* **25**(11), 2061–2086. doi: 10.1080/01431160310001647697.

Makynen MP, Manninen AT, Simila MH, Karvonen JA and Hallikainen MT (2002) Incidence angle dependence of the statistical properties of C-band HH-polarization backscattering signatures of the Baltic Sea ice. *IEEE Transactions on Geoscience and Remote Sensing* **40**(12), 2593–2605. doi: 10.1109/TGRS.2002.806991.

Martinez-Agirre A, Álvarez-Mozos J, Lievens H, Verhoest NEC and Giménez R (2017) Influence of surface roughness sample size for C-band SAR backscatter applications on agricultural soils. *IEEE Geoscience and Remote Sensing Letters* **14**(12), 2300–2304. doi: 10.1109/LGRS.2017.2762434.

Melling H (1998) Detection of features in first-year pack ice by synthetic aperture radar (SAR). *International Journal of Remote Sensing* **19**(6), 1223–1249. doi: 10.1080/014311698215702.

Milillo P, Riel B, Minchew B, Yun S-H, Simons M and Lundgren P (2015) On the synergistic use of SAR constellations' data exploitation for earth science and natural hazard response. *IEEE Journal of Selected Topics in Applied Earth Observations and Remote Sensing* **PP**(99), 1–6. doi: 10.1109/JSTARS.2015.2465166.

Moen M-AN, Doulgeris AP, Anfinsen SN, Renner AHH, Hughes N, Gerland S and Eltoft T (2013) Comparison of feature based segmentation of full polarimetric SAR satellite sea ice images with manually drawn ice charts. *The Cryosphere* **7**(6), 1693–1705. doi: 10.5194/tc-7-1693-2013.

Mussells O (2015) Observing pressured sea ice in the Hudson Strait using RADARSAT: Implications for shipping. Thesis, Université d'Ottawa / University of Ottawa. http://www.ruor.uottawa.ca/handle/10393/33358.

Nasonova S, Scharien RK, Geldsetzer T, Howell SEL and Power D (2018) Optimal compact polarimetric parameters and texture features for discriminating sea ice types during winter and advanced melt. *Canadian Journal of Remote Sensing* **44**(4), 390–411. doi: 10.1080/07038992.2018.1527683.

Nghiem SV, Rigor IG, Perovich DK, Clemente-Colón P, Weatherly JW and Neumann G (2007) Rapid reduction of Arctic perennial sea ice. *Geophysical Research Letters* **34**(19). doi: 10.1029/2007GL031138.

Nolin AW, Fetterer FM and Scambos TA (2002) Surface roughness characterizations of sea ice and ice sheets: case studies with MISR data. *IEEE Transactions on Geoscience and Remote Sensing* **40**(7), 1605–1615. doi: 10.1109/TGRS.2002.801581.

Nolin AW and Mar E (2019) Arctic sea ice surface roughness estimated from multi-angular reflectance satellite imagery. *Remote Sensing* **11**(1), 50. doi: 10.3390/rs11010050.

Nolin AW and Payne MC (2007) Classification of glacier zones in western Greenland using albedo and surface roughness from the Multi-angle Imaging SpectroRadiometer (MISR). *Remote Sensing of Environment* **107**(1–2), 264–275. doi: 10.1016/j.rse.2006.11.004.

Remund QP and Long DG (2014) A decade of QuikSCAT scatterometer sea ice extent data. *IEEE Transactions on Geoscience and Remote Sensing* **52**(7), 4281–4290. doi: 10.1109/TGRS.2013.2281056.

Richards JA (2009) *Remote sensing with imaging radar.* Springer Berlin Heidelberg, Berlin, Heidelberg. doi: 10.1007/978-3-642-02020-9.

Segal RA, Scharien RK, Duerden F and Tam C-L (*in press*) The best of both worlds - Connecting remote sensing and Arctic communities for safe sea ice travel. *Arctic.*

Shean DE, Alexandrov O, Moratto ZM, Smith BE, Joughin IR, Porter C and Morin P (2016) An automated, open-source pipeline for mass production of digital elevation models (DEMs) from very-high-resolution commercial stereo satellite imagery. *ISPRS Journal of Photogrammetry and Remote Sensing* **116**, 101–117. doi: 10.1016/j.isprsjprs.2016.03.012.

Shepherd A, Ivins ER, A G, Barletta VR, Bentley MJ, Bettadpur S, Briggs KH, Bromwich DH, Forsberg R, Galin N, Horwath M, Jacobs S, Joughin I, King MA, Lenaerts JTM, Li J, Ligtenberg SRM, Luckman A, Luthcke SB, McMillan M, Meister R, Milne G, Mouginot J, Muir A, Nicolas JP, Paden J, Payne AJ, Pritchard H, Rignot E, Rott H, Sørensen LS, Scambos TA, Scheuchl B, Schrama EJO, Smith B, Sundal AV, Angelen JH van, Berg WJ van de, Broeke MR van den, Vaughan DG, Velicogna I, Wahr J, Whitehouse PL, Wingham DJ, Yi D, Young D and Zwally HJ (2012) A reconciled estimate of ice-sheet mass balance. *Science* **338**(6111), 1183–1189. doi: 10.1126/science.1228102.

Similä M, Mäkynen M and Heiler I (2010) Comparison between C band synthetic aperture radar and 3-D laser scanner statistics for the Baltic Sea ice. *Journal of Geophysical Research: Oceans* **115**(C10). doi: 10.1029/2009JC005970.

Wu Y, Gong P, Liu Q and Chappell A (2009) Retrieving photometric properties of desert surfaces in China using the Hapke model and MISR data. *Remote Sensing of Environment* **113**(1), 213–223. doi: 10.1016/j.rse.2008.09.006.

Xu L, Clausi DA, Li F and Wong A (2017) Weakly supervised classification of remotely sensed imagery using label constraint and edge penalty. *IEEE Transactions on Geoscience and Remote Sensing* **55**(3), 1424–1436. doi: 10.1109/TGRS.2016.2623942.

Yitayew TG, Dierking W, Divine DV, Eltoft T, Ferro-Famil L, Rösel A and Negrel J (2018) Validation of sea-ice topographic heights derived from TanDEM-X interferometric SAR data with results from laser profiler and photogrammetry. *IEEE Transactions on Geoscience and Remote Sensing* **56**(11), 6504–6520. doi: 10.1109/TGRS.2018.2839590.

Zakharov I, Bobby P, Power D, Saunders K and Warren S (2015) Monitoring hazardous sea ice features using satellite imagery. *Offshore Technology Conference*, Copenhagen, Denmark. doi: 10.4043/25570-MS.